

# GeodesicPSIM: Predicting the Quality of Static Mesh with Texture Map via Geodesic Patch Similarity

Qi Yang, Joel Jung, Xiaozhong Xu, *Member, IEEE*, and Shan Liu, *Fellow, IEEE*

**Abstract**—Static meshes with texture maps have attracted considerable attention in both industrial manufacturing and academic research, leading to an urgent requirement for effective and robust objective quality evaluation. However, current model-based static mesh quality metrics have obvious limitations: most of them only consider geometry information, while color information is ignored, and they have strict constraints for the meshes’ geometrical topology. Other metrics, such as image-based and point-based metrics, are easily influenced by the preprocessing algorithms, e.g., projection and sampling, hampering their ability to perform at their best. In this paper, we propose Geodesic Patch Similarity (GeodesicPSIM), a novel model-based metric to accurately predict human perception quality for static meshes. After selecting a group keypoints, 1-hop geodesic patches are constructed based on both the reference and distorted meshes cleaned by an effective mesh cleaning algorithm. A two-step patch cropping algorithm and a patch texture mapping module refine the size of 1-hop geodesic patches and build the relationship between the mesh geometry and color information, resulting in the generation of 1-hop textured geodesic patches. Three types of features are extracted to quantify the distortion: patch color smoothness, patch discrete mean curvature, and patch pixel color average and variance. To the best of our knowledge, GeodesicPSIM is the first model-based metric especially designed for static meshes with texture maps. GeodesicPSIM provides state-of-the-art performance in comparison with image-based, point-based, and video-based metrics on a newly created and challenging database. We also prove the robustness of GeodesicPSIM by introducing different settings of hyperparameters. Ablation studies also exhibit the effectiveness of three proposed features and the patch cropping algorithm. The code is available at <https://multimedia.tencent.com/resources/GeodesicPSIM>.

**Index Terms**—Static mesh with texture map, Objective quality assessment, Geodesic patch

## I. INTRODUCTION

A 3D mesh is a collection of vertices in the 3D space, connected through edges that compose polygonal faces. With additional attributes, such as normal vectors and texture coordinates, static meshes are widely used in many areas, such as gaming, animation, medical imaging, and industrial manufacturing. The 3D mesh and the 3D point cloud, which is another type of prevalent 3D media consisting of scattered points, are mutually convertible as illustrated in Fig. 1. The differences are that 3D meshes have a regular topology and a continuous surface, which can be transformed geometrically and textured, leading to a flexible and efficient rendering. Due

to their unique characteristics, static meshes attract considerable attention in modern industrial design, such as rapid prototyping, digital fabrication, and precision measurement, and also become a hotspot for academic research.

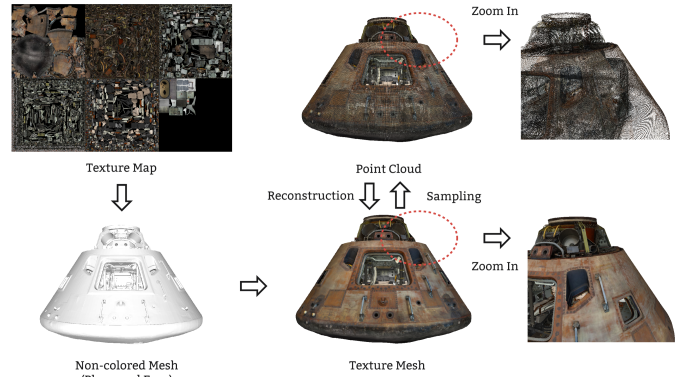


Fig. 1: Snapshots of reference meshes in TSMD.

Static meshes can be divided into three types regarding the texture form: non-colored mesh, colored mesh with vertex texture, and colored mesh with texture map. In this paper, we focus on static meshes with texture maps due to their common wide utilization in academic and industrial fields.

Given the substantial volume of static mesh data, static mesh compression emerges as an extremely important and unavoidable technology [1], raising new requirements for the quality evaluation of static meshes in terms of lossy compression [2], [3], as illustrated in Fig. 2. Rate-distortion (RD) curves are used to measure compression efficiency [4], which means a reliable quality evaluation can help to select a superior codec tool, select an optimal compression configuration, and save bandwidth and other resource costs.

Undoubtedly, the most reliable quality evaluation method is to conduct subjective experiments, collecting enough subjective scores to calculate mean opinion scores (MOS). However, the subjective experiment is expensive, time-consuming, and requires a rigorous testing environment, leading to extreme inconvenience in practical applications. Therefore, an effective and robust objective metric is needed to replace subjective experiments and facilitate the study of mesh compression.

Objective quality assessment of static meshes has made significant progress since a series of model-based metrics are suggested to quantify the distortion of static mesh geometry by introducing structure features, such as curvature [5], smooth-

Q. Yang, J. Jung, X. Xu, S. Liu are from Tencent Media Lab, China/France/USA, (e-mail: {chinoyang, joeljung, xiaozhongxu, shanliu}@tencent.com)

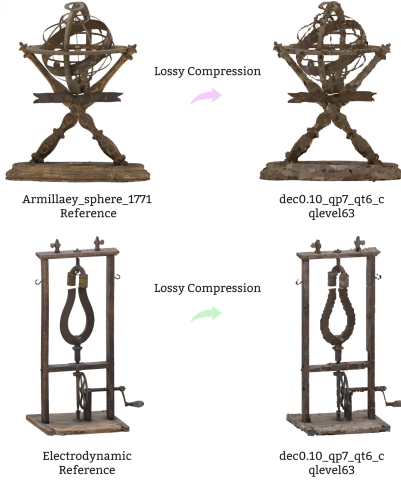


Fig. 2: Snapshots of lossy compressed meshes. "dec", "qp", "qt", and "qlevel" are compression parameters defined in section III.

ness [6], [7], dihedral angles [8], etc., showing better correlations with human perception than metrics based on point-wise features [9]. However, these earlier model-based metrics are not sufficiently robust to handle the complexities involved in current static mesh quality evaluation tasks for the following reasons: first, these metrics only consider geometry features, targeting the non-colored static meshes, while currently, the textured static meshes are the spotlight due to broader application scenarios; second, they have strict constraints regarding the meshes' geometrical topology, requiring both the reference and the distorted mesh have perfect manifold surface and share the same vertex density, the same connectivity, or the same level of details. Therefore, the appearance of new demands has spurred research into objective static mesh quality assessment. In this paper, we focus on the full-reference metric, in which the reference mesh is provided as evidence to assist in the quality prediction of distorted meshes.

Given the rapid development in the fields of image and point cloud quality assessment, WG7 - MPEG Coding of 3D Graphics and Haptics proposed two strategies to measure static mesh quality, i.e., image-based and point-based metrics [10]. Some research also suggested using rendered mesh videos to infer mesh quality [11]. These methods all need to convert the static meshes into other media formats, such as image, point cloud, and video, by some preprocessing algorithms like projection and sampling, which unavoidably introduce errors and hamper the metrics' ability to perform at their best. For instance, projected images may contain background information that can mask the influence of distortion and reduce metric performance. In addition, preprocessing algorithms require extra computational resource overhead, such as rendering of static mesh needs extra time, and sampling methods typically operate on faces in a per-face manner.

In light of the above analysis and explanation, it can be concluded that an effective and robust model-based metric, targeting static meshes with texture maps that undergo different types of distortion, needs to be designed. Four key problems

need to be considered for effective full-reference model-based metrics. First, either reference or distorted mesh may have redundant and invalid information. Removing this information while maintaining mesh visual fidelity is the basis for ensuring the validity and stability of subsequent processing. Second, a simple and accurate method is important to build a local area correspondence between the reference meshes and the distorted meshes. It can facilitate the extraction of structural features by injecting the appropriate information. For other media types, such as image and point cloud, the local area correspondence can be easily established by pixel windows [12], [13] or keypoint neighborhoods [14], [15]. However, the fundamental elements of the mesh are irregular polygons. Directly using raw polygons to build local area correspondence might cause position offset and size mismatch, consequently leading to the mismatch of features. Third, information from the texture map needs to be extracted corresponding to each local area. Although texture coordinates are provided for mesh vertices, the texture inside the face also needs to be taken into consideration. Fourth, designing effective geometry and color feature extraction methods is the guarantee of accurate quality prediction results. The calculation of features should not strictly require the topology of reference and distorted meshes, and the features should be sensitive to mesh distortions.

In this paper, we propose an effective model-based metric, called Geodesic Patch Similarity (GeodesicPSIM), inspired by multidisciplinary research such as neuroscience, graph signal processing (GSP), and conformal geometry. GeodesicPSIM is the first model-based metric especially designed for static mesh with texture map, solving the four key problems mentioned above by thoughtfully designed effective algorithms. First, a mesh cleaning algorithm is proposed to solve the first key problem, which can detect and remove redundant and invalid information such as duplicated vertices, null faces, etc. Second, a cluster of keypoints is selected, centered on which a group of 1-hop geodesic patches is constructed as feature extraction units. Third, a two-step patch cropping algorithm is proposed to resize 1-hop geodesic patches to a suitable size, addressing the second key problem and optimizing feature extraction. Subsequently, a patch texture mapping module is proposed to generate 1-hop textured geodesic patches. Effective pixels, derived from the texture map, are extracted for each face contained in 1-hop geodesic patches, tackling the third key problem. Finally, three types of features, i.e., patch color smoothness, patch discrete mean curvature, and patch pixel color average and variance, are proposed to quantify the influence of mesh distortion and address the last key problem. Patch color smoothness and discrete mean curvature are inspired by the observations in neuroscience that the human visual system is sensitive to high-frequency distortion [15], [16] and processes color and form information separately [17]. Patch pixel color average and variance are proposed to quantify the distortion within each face, in which the effective pixels of each face are extracted from the texture map. GeodesicPSIM scores are calculated by combining all feature similarities with a simple method.

To prove the superiority of GeodesicPSIM, a newly created and challenging static mesh quality assessment database,

called TSMD, is introduced. Then GeodesicPSIM and 16 other state-of-the-art (SOTA) metrics are evaluated on TSMD. Three correlation indicators are reported, including Pearson's linear correlation coefficient (PLCC), Spearman's rank order correlation coefficient (SRCC), and root mean square error (RMSE). The experimental results suggest the reliable and superior performance of GeodesicPSIM in MOS prediction for TSMD with PLCC, SRCC, and RMSE at 0.82, 0.82 and 0.66, which is the first in all metrics. The robustness of GeodesicPSIM is also examined by adjusting the selection of hyperparameters, revealing that GeodesicPSIM presents stable and predictable performance variations in various scenarios. Ablation studies demonstrate the importance and necessity of feature pooling and patch cropping. The main contribution of this paper is summarized as follows:

- to our knowledge, the proposed GeodesicPSIM is the first model-based metric especially designed for static mesh with texture map. We solve the key problems of quality assessment for static mesh with texture map and propose three types of features for robust, effective quality prediction.
- we test GeodesicPSIM using a newly created and challenging database, exhibiting the SOTA results in MOS prediction.
- we perform extensive experiments to show the robustness and generalizations of GeodesicPSIM.

The remainder of this paper is as follows. Section II presents the related work about mesh objective quality metrics. Section III introduces the database used to evaluate objective metrics, reporting the weaknesses of SOTA metrics. Section IV details the design of GeodesicPSIM. Section V illustrates the experimental results and analyzes the robustness and generalization of GeodesicPSIM. Section VI concludes the article and highlights future work.

## II. RELATED WORK

Objective quality evaluation for static mesh has been studied for decades, it can be roughly divided into four types: image-based, point-based, video-based, and model-based metrics.

Image-based, point-based, and video-based metrics all require preprocessing algorithms before quality prediction, that is, converting static meshes into other media formats like images, processed video sequences (PVSS), and point clouds, and then using mature and well-accepted metrics with their respective fields to infer quality. Image-based metrics use multiple projected images from static meshes with different viewpoints as evidence serving the metrics such as  $geo_{psnr}$  [10],  $rgb_{psnr}$ , etc. Point-based metrics first sample the static meshes via classical sampling algorithms, such as grid sampling, face sampling, surface subdivision sampling, etc., then the SOTA point cloud objective metrics are involved to predict quality scores: point-to-point (D1) [18], point-to-plan (D2) [19], PCQM [20], MS-GraphSIM [21], etc. Video-based metrics first define a smooth camera path to capture continuous images to generate PVS, then image/video quality assessment (IQA/VQA) metrics are utilized to infer quality, such as SSIM [22], MSSIM [12], and VMAF [23]. However, the

preprocessing algorithms required by the above metrics may incur unexpected bias, hampering the metrics' ability to show their best performance.

Unlike the above-mentioned three methods, model-based metrics do not need media type conversion, they directly use the raw data of the static mesh to extract features and predict the quality. From the earliest point-to-mesh [9], based on point-wise features, to metrics using structure features such as MSDM [5], DWPM [6], and GL [7], model-based metrics gradually show better performance by taking into account more and more characteristics of the human visual system. For example, MSDM [5] introduced a surface curvature to quantify mesh quality. DWPM [6] made use of global roughness to measure the distortion of the mesh surface. DAME [8] detected variations in the structure of the mesh geometry based on the estimation of dihedral angles. GL [7] proposed another method for calculating surface smoothness using the geometric Laplacian of vertices.

However, the model-based metrics cited above only consider geometry distortions while texture distortions are ignored. Consequently, it leads to an inadequate quality prediction considering texture information that might mask the characteristics of geometry [24], [25]. In addition, they also have strict constraints on distorted meshes, such as sharing the same connectivity, the same vertex density, or the same level of detail [10]. Duplicated vertices, duplicated faces, and null faces can even affect the normal operation of the metrics, indicating that they have poor tolerance for invalid and interference information, which limits the metrics' performance in real applications. Therefore, a new effective and robust metric is needed to facilitate the study of mesh compression and other visual quality-related tasks.

## III. TSMD-A CHALLENGING STATIC MESH QUALITY ASSESSMENT DATABASE

In this section, a newly created database with rich content, reliable MOSs, and usefully supplementary materials (PVSs and bitrate), called TSMD, is introduced [26]<sup>1</sup>. Due to the diversity of distorted meshes, the SOTA metrics only achieve a correlation of around 0.75, serving as a catalyst for the GeodesicPSIM study.

### A. Database Creation

1) *Content description*: TSMD compiled 42 publicly available meshes from reputable sources, which encompass a rich category of static meshes, such as human characters, animals, plants, buildings, indoor scenes, inanimate objects, etc. The essential information of the database is summarized in Table I.

2) *Distortion generation*: Four distinct types of distortion are successively introduced into the reference meshes, corresponding to the distortion applied in the context of the VVM polygonal static mesh coding Call for Proposals (CfP) of AOMedia [1] depicted in Fig. 3, and generate 210 distorted meshes.

Each mesh successively undergoes dequantization, triangulation, decimation, encoding, and decoding with Draco. Each

<sup>1</sup><https://multimedia.tencent.com/resources/tsmd>.

TABLE I: Summary information of the TSMD.

Number of meshes	42
Distortions applied to the mesh (successively)	Dequantization, Triangulation, Decimation, Draco compression
Distortions applied to the texture (successively)	Downscaling, AV1 (libaom) compression
Levels of distortion	5
Total number of distorted meshes	210
Total number of scores collected via crowdsourcing	10320
Remaining scores after outlier removal	9468

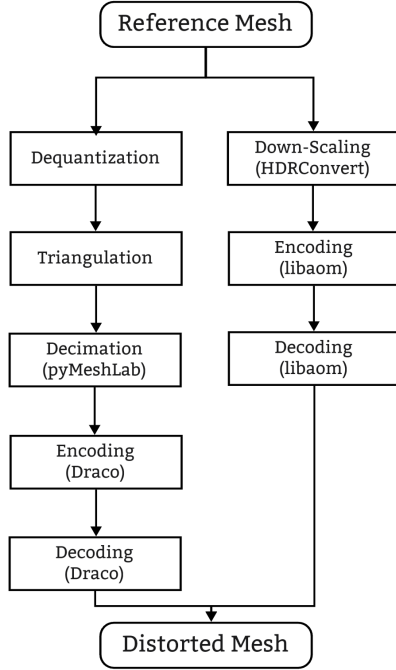


Fig. 3: Static mesh compression anchor.

texture map is downscaled to meet the following criteria: the vertical/horizontal ratio is maintained, and neither the horizontal nor the vertical resolution exceeds 4096 pixels. Subsequently, AV1 compression is applied. For each distortion, five encoding configurations are chosen, consisting of the following parameters: decimation level (dec), Draco quantization parameter for position attribute (qp) and for the texture attribute (qt) (normals are not quantized), and AV1 quantization (cqlevel). This allows us to achieve five RD points, evenly spread across practical quality ranges that are applicable to various use cases.

3) *PVS generation*: Processed Video Sequences (PVSs) are generated from both source and distorted content using a conventional approach. These 2D videos depict camera paths that simulate typical user motions and are displayed during subjective tests to enable the evaluation process. The open3D library is used to render the content from distorted meshes and textures. The object is centered, and its size is adjusted to occupy a significant portion of the frame. A rotational movement is applied to the object, following a cosine function

that gradually decreases the rotation speed until near stop and then increases it again. For two meshes that represent scenes inside a building, the camera is positioned inside the scene before the rotational movement is applied. The resulting PVSs are created with a frame rate of 30 fps and a duration of 18 seconds and are encoded using the FFMPEG library, with the x264 encoder and a constant rate factor equal to 10 to ensure visually lossless encoding. This approach is in line with the guidelines proposed in [27].

4) *Subjective experiment*: A crowdsourcing methodology is employed to conduct subjective tests, which involves a proprietary interface for downloading and streaming the PVS to participants. Before the rating session begins, instructions are given to ensure the clarity and consistency of the test. Additionally, a training session is conducted to replicate the rating session, where participants are asked to assign scores within the range of "possible" scores for 8 PVS, excluding any unrealistic scores. This serves as a qualification criterion for the actual rating session. The methodology follows the ITU-T P.910 Recommendation [28] and is adapted to the crowdsourcing approach. A double-stimulus impairment scale is used, where the source content and the distorted content are shown in pairs, in random order, before the score is requested, using a five-level scale to rate the impairments. The participants are "naïve" viewers, not familiar with research related to meshes, and consist of 74 students aged 17 to 25 years.

5) *Outlier detection*: In the realm of crowdsourcing, the detection and elimination of outliers is of the utmost importance. To tackle this problem, certain "trapping" PVS are deliberately included in the rating sessions. These PVS can be divided into two categories: 1- extremely low-quality PVS, for which extremely low scores are expected, and 2- duplicated PVS, for which close scores are anticipated. By incorporating these trapping PVS, it is possible to identify and filter out any outliers during the evaluation process. In addition, the correlation between the average score and each group of raw data is calculated. If the correlation value is below 0.8, the corresponding data are considered unreliable and are consequently excluded from the database. As a result, 852 scores were removed from a total of 10320. It is ensured that each PVS has a remaining number of scores above 15 to compute the Mean Opinion Score (MOS), once outliers are eliminated.

### B. Database validation

The diversity of content and the accuracy of MOS are hereby comprehensively discussed and summarized to facilitate the presentation of key information.

First, to measure the diversity of the database, spatial information (SI) and temporal information (TI) are calculated based on PVS and are illustrated in Fig. 4. Both indicators reveal the difference in geometry and texture characteristics of 3D meshes under different viewpoints. The indoor scene meshes (e.g., the\_great\_drawing\_room), enrich the diversity of content in terms of spatial information significantly.

Second, to verify the MOS accuracy of the database, the correlations between MOS and bitrate are carefully examined.



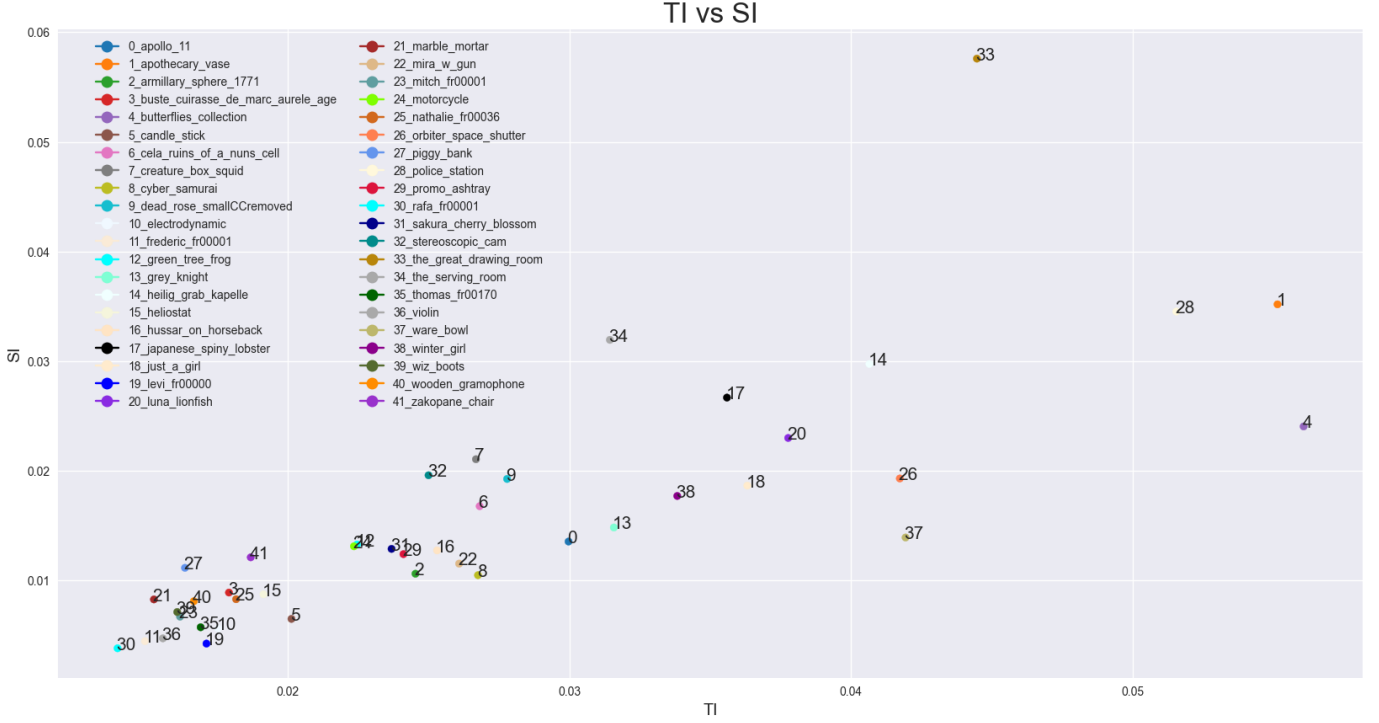


Fig. 4: SI vs TI for TSMD.

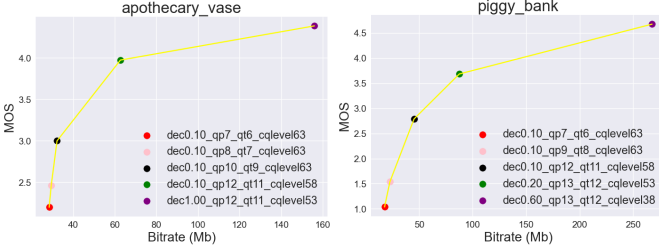


Fig. 5: Example of monotonic bitrate vs MOS curves.

Most bitrate vs MOS curves show perfect monotony as shown in Fig. 5, satisfying the intuition that a higher bitrate that provides more delicate visual information should have a higher MOS. Some meshes with MOS values are illustrated in Fig. 6.

### C. SOTA metric performance on TSMD

The results of eight SOTA objective metrics, that is, two image-based metrics,  $geo_{psnr}$  [10] and  $yuv_{psnr}$  [10], three point-based metrics, D1 [18], D2 [19], and  $PCQM_{psnr}$  [20] [10], three video-based metrics, PSNR, SSIM [22], and VMAF [23], are reported in Table II, in which the best is  $PCQM_{psnr}$  [20] achieving a correlation around 0.75.

### D. Summary

TSMD provides diverse content and reliable MOS. However, the best metrics are shown to only achieve a correlation of around 0.75 because of the heterogeneous nature of TSMD. Previous research often reports high PLCC and SRCC correlations (around 0.9) for the top-performing metrics, indicating



Fig. 6: Illustration of meshes with MOSs.

that TSMD is a challenging database and motivating the design of new metrics.

## IV. GEODESICPSIM: A MODEL-BASED METRIC FOR MESH QUALITY ASSESSMENT

In this section, the construction of GeodesicPSIM is introduced. It consists of seven steps: mesh cleaning, keypoint

TABLE II: Metric Performance on TSMD

Metric	PLCC	SRCC	RMSE
geOpsnr	0.73	0.73	0.80
yuvpsnr	0.68	0.68	0.85
D1	0.72	0.65	0.80
D2	0.54	0.47	0.98
PCQM <sub>psnr</sub>	<b>0.76</b>	<b>0.75</b>	<b>0.76</b>
PSNR	0.53	0.54	0.99
SSIM	0.51	0.67	0.85
VMAF	0.70	0.51	1.00

selection, 1-hop geodesic patch construction, patch cropping, patch texture mapping, feature extraction, and feature pooling. Fig. 7 illustrates the GeodesicPSIM flowchart.

#### A. Mesh cleaning

Different from traditional 2D media, such as images and videos, both reference and distorted meshes are often accompanied by redundant and invalid information, which is generally visually useless but increases computation complexity of metric and even interferes with feature extraction, such as duplicated vertices, null faces, etc. To ensure the stability of the metric, we propose a mesh cleaning algorithm based on visual fidelity as the first step of GeodesicPSIM. First, duplicated and unreferenced vertices are detected and removed from the vertex matrix. Second, the vertex indexes are updated for the face matrix, after which duplicated and null faces are detected and removed from the face matrix. Based on the new vertex and face matrix, the texture matrix is updated. Repeat the above two steps until no duplicated or unreferenced vertices are detected.

For better understanding, the subscripts  $r$  and  $d$  are used to indicate the content of reference and distorted meshes in the following sections, while no subscript means the operand/processing is general for both the reference and distorted meshes/objects.

Mathematically, for a mesh,  $\hat{\mathbf{M}}$ , the vertex matrix, face matrix, texture matrix are defined as  $\hat{\mathcal{M}}_{\mathbf{V}} \in \mathbb{R}^{v' \times 3}$ ,  $\hat{\mathcal{M}}_{\mathbf{F}} \in \mathbb{R}^{f' \times 3}$ ,  $\hat{\mathcal{M}}_{\mathbf{T}} \in \mathbb{R}^{v' \times 2}$ , the cleaned mesh,  $\mathbf{M}$ , can be generated using **Algorithm 1**.

#### B. Keypoint selection

Keypoint is used to build local area correspondence between reference and distorted meshes. Similar method has been utilized in point cloud full-reference metrics [15] [20] [29]. Point clouds can easily add a pseudo vertex/point as keypoint to realize precise local area matching, since the units of the point cloud are scattered points that do not have connections. However, static meshes have a fixed geometry structure with polygonal face as unit. Merging a new pseudo vertex to a surface without affecting the geometry is a relatively complex problem.

To simplify the above problem, we propose selecting keypoints based on mesh vertices. For typical mesh distortions, such as lossy compression, there are some operands, such as mesh decimation, that will reduce the number of vertices, resulting in the distorted meshes having sparser vertex distributions while having larger face size than the reference meshes

---

#### Algorithm 1 Mesh cleaning

---

**Input:** The raw mesh,  $\hat{\mathbf{M}}$ , including vertex matrix  $\hat{\mathcal{M}}_{\mathbf{V}} \in \mathbb{R}^{v' \times 3}$ , face matrix  $\hat{\mathcal{M}}_{\mathbf{F}} \in \mathbb{R}^{f' \times 3}$ , and texture matrix  $\hat{\mathcal{M}}_{\mathbf{T}} \in \mathbb{R}^{v' \times 2}$

**Output:** the cleaned mesh,  $\mathbf{M}$ , including vertex matrix  $\mathcal{M}_{\mathbf{V}} \in \mathbb{R}^{v \times 3}$ , face matrix  $\mathcal{M}_{\mathbf{F}} \in \mathbb{R}^{f \times 3}$ , and texture matrix  $\mathcal{M}_{\mathbf{T}} \in \mathbb{R}^{v \times 2}$

- 1: Detecting duplicated vertex  $\mathbf{Dv}$  and unreferenced vertex  $\mathbf{Uv}$
  - 2: **while**  $\mathbf{Dv} \cup \mathbf{Uv} \neq \emptyset$  **do**
  - 3:   Removing the duplicated vertex and unreferenced vertex
  - 4:   Updating the vertex index in face matrix  $\hat{\mathcal{M}}_{\mathbf{F}}$ , updating the texture matrix  $\hat{\mathcal{M}}_{\mathbf{T}}$  corresponding to vertex matrix
  - 5:   Detecting duplicated face  $\mathbf{Df}$  and null face  $\mathbf{Nf}$
  - 6:   **if**  $\mathbf{Df} \cup \mathbf{Nf} \neq \emptyset$  **then**
  - 7:     Removing duplicated face and null face
  - 8:   **end if**
  - 9:   Detecting duplicated vertex  $\mathbf{Dv}$  and unreferenced vertex  $\mathbf{Uv}$
  - 10: **end while**
- 

[30] [1]. A vertex, which coordinates copied from a certain vertex belong to the distorted mesh, might help to find a closer neighbor from the reference mesh vertex cluster, minimizing the shifting of local area matching. Therefore, we use sampling to select vertices from distorted mesh as keypoints, formulated as

$$\mathcal{K} = \phi[\mathcal{M}_{\mathbf{V}_d}]_{kn} \in \mathbb{R}^{kn \times 3}. \quad (1)$$

$\phi[*]_{kn}$  samples  $kn$  points from the distorted mesh vertex matrix  $\mathcal{M}_{\mathbf{V}_d}$ , generating the keypoint set  $\mathcal{K}$ .

#### C. 1-hop geodesic patch construction

The geometry information of static mesh is a natural 3D graph with vertices as graph nodes and faces to indicate graph edges. In GSP, if there is an edge between two vertices, then the two vertices are 1-hop neighbors to each other [31]. 1-hop geodesic patch consists of faces with 1-hop neighbors as vertices, exhibiting a mesh local geometry attribute. Given the cleaned reference and distorted meshes,  $\mathbf{M}_r$  and  $\mathbf{M}_d$ , for  $k_i \in \mathcal{K}$ , KNN search is first used to find  $k_i$ 's nearest neighbor in the reference and distorted meshes,  $k_{ri} \in \mathcal{M}_{\mathbf{V}_r}$  and  $k_{di} \in \mathcal{M}_{\mathbf{V}_d}$ . Regarding the index of  $k_{ri}$  and  $k_{di}$  in  $\mathcal{M}_{\mathbf{F}_r}$  and  $\mathcal{M}_{\mathbf{F}_d}$ , the 1-hop neighbors of  $k_{ri}$  and  $k_{di}$  can be easily extracted that appropriate for constructing 1-hop geodesic patch, i.e.,

$$\begin{aligned} \mathcal{V}_{(v_r, k_{ri})} &= \{v_r\} \subset \mathcal{M}_{\mathbf{V}_r}, (v_r, k_{ri}) \in \mathcal{M}_{\mathbf{F}_r}, \\ \mathcal{V}_{(v_d, k_{di})} &= \{v_d\} \subset \mathcal{M}_{\mathbf{V}_d}, (v_d, k_{di}) \in \mathcal{M}_{\mathbf{F}_d}. \end{aligned} \quad (2)$$

$\mathcal{V}_{(v_r, k_{ri})}$  and  $\mathcal{V}_{(v_d, k_{di})}$  represent the 1-hop neighbors of  $k_{ri}$  and  $k_{di}$  in reference and distorted meshes.  $(v, k) \in \mathcal{M}_{\mathbf{F}}$  indicates vertices  $v$  and  $k$  form an edge of one or more faces collected by  $\mathcal{M}_{\mathbf{F}}$ .

Two toy examples of 1-hop geodesic patches are illustrated in Fig. 7. Reference and distorted 1-hop geodesic patches

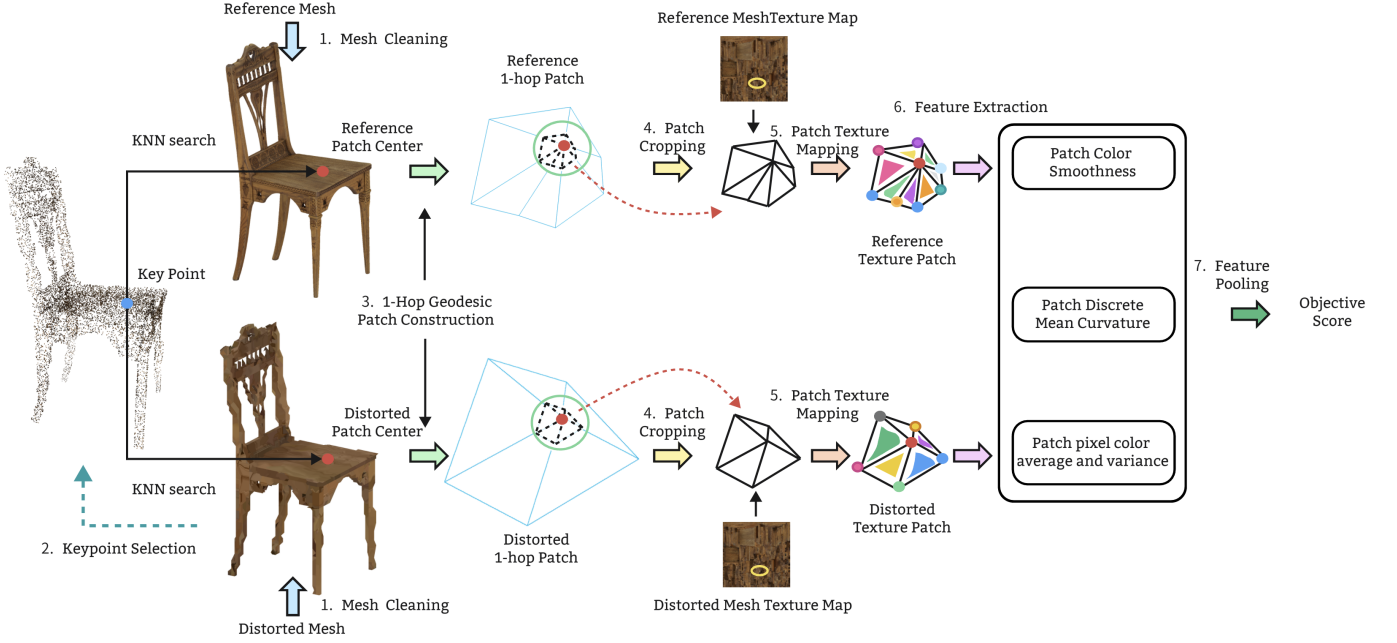


Fig. 7: Flowchart of GeodesicPSIM.

centered with  $k_{ri}$  and  $k_{di}$  are recorded that  $\mathbf{G}_{k_{ri}, \mathbf{M}_r}$  and  $\mathbf{G}_{k_{di}, \mathbf{M}_d}$ , with  $\mathcal{V}_{(v_r, k_{ri})}$  and  $\mathcal{V}_{(v_d, k_{di})}$  to construct the faces  $\mathcal{F}_{\mathcal{V}_{(v_r, k_{ri})}}$  and  $\mathcal{F}_{\mathcal{V}_{(v_d, k_{di})}}$ , i.e.,  $\mathbf{G}_{k_{ri}, \mathbf{M}_r} = \mathcal{V}_{(v_r, k_{ri})} \oplus \mathcal{F}_{\mathcal{V}_{(v_r, k_{ri})}}$  and  $\mathbf{G}_{k_{di}, \mathbf{M}_d} = \mathcal{V}_{(v_d, k_{di})} \oplus \mathcal{F}_{\mathcal{V}_{(v_d, k_{di})}}$ .

#### D. Patch cropping

Patch cropping aims to crop the 1-hop geodesic patches to a predefined size, facilitating the extraction of effective features.

There are two reasons to perform patch cropping. First, the reference and distorted 1-hop geodesic patches may cover areas of different sizes. For example, after mesh decimation, the decimated meshes usually have larger face sizes, resulting the distorted 1-hop geodesic patch includes exclusive information that is out of coverage of the reference 1-hop geodesic patch. Second, the initial face size for different source meshes or different areas of the same source meshes might also be different, while structure features are generally sensitive to the size of the feature extraction unit.

Referring to the study on neuroscience and quality assessment [22], [32]–[34], the perceptual visual signal can be simulated using a low-pass filter to aggregate information from the retina, indicating that the processing unit of the human visual system is limited in an area centered at the viewpoint. Excessively large patch sizes can weaken the effectiveness of feature extraction, consequently resulting in a deviation of human perception prediction.

Therefore, we propose a two-step patch cropping method shown in **Algorithm 2**: the cropping step 1 ensures that the size of the distorted 1-hop geodesic patch cannot be significantly larger than the reference one, and the cropping step 2 ensures that the size of both the reference and distorted patches cannot be greater than a predefined threshold  $\tau$ . This cropping algorithm shrinks the 1-hop geodesic patch by generating pseudo 1-hop neighbors based on the original neighbors,

resulting in similar polygons before and after cropping, which will not change the overall patch geometry characteristics. An example of patch cropping is illustrated in Fig. 7, highlighted by the red dashed lines.

#### Algorithm 2 Mesh Patch Cropping

**Input:** The initial reference and distorted 1-hop geodesic patches,  $\mathbf{G}_{k_{ri}, \mathbf{M}_r}$  and  $\mathbf{G}_{k_{di}, \mathbf{M}_d}$ , a threshold  $\tau$

**Output:** The cropped reference and distorted 1-hop geodesic patches,  $\mathbf{G}'_{k_{ri}, \mathbf{M}_r}$  and  $\mathbf{G}'_{k_{di}, \mathbf{M}_d}$

- 1: Calculating the average Euclidean distance from the 1-hop neighbors to the patch center, i.e.,  $D_r = \frac{1}{|v_r|} \sum_{v_r^j \in \mathcal{V}_{v_r, k_{ri}}} \|v_r^j - k_{ri}\|_2$ ,  $D_d = \frac{1}{|v_d|} \sum_{v_d^j \in \mathcal{V}_{v_d, k_{di}}} \|v_d^j - k_{di}\|_2$
- 2: **Cropping step 1**
- 3: **if**  $(D_d/D_r = t) > 1$  **then**
- 4: Cropping the distorted 1-hop geodesic patch  $\mathbf{G}_{k_{di}, \mathbf{M}_d}$ : generating the pseudo 1-hop neighbors  $\mathbf{V}'_{v_d, k_{di}} = \{\frac{v_d^j - k_{di}}{t} + v_d^j\}$ , generating the texture coordinates for  $\mathbf{V}'_{v_d, k_{di}}$  with the same method
- 5: **end if**
- 6: **Cropping step 2**
- 7: **if**  $(D_r/\tau = l) > 1$  **then**
- 8: Cropping the reference and distorted 1-hop geodesic patches:  $\mathbf{V}'_{v_r, k_{ri}} = \{\frac{v_r^j - k_{ri}}{\tau} + v_r^j\}$ ,  $\mathbf{V}'_{v_d, k_{di}} = \{\frac{v_d^j - k_{di}}{\tau} + v_d^j\}$ , generating the texture coordinates for  $\mathbf{V}'_{v_r, k_{ri}}$  and  $\mathbf{V}'_{v_d, k_{di}}$ , accordingly.
- 9: **end if**

#### E. Patch texture mapping

Geodesic patches only provide geometry information, i.e., vertex and face, it is not what the human eye actually perceives

under actual viewing conditions, leading to the proposal of patch texture mapping.

Generally, a texture coordinate is a pair of floating numbers between 0 and 1 noted as  $(u, v)$ , given the pixel matrix of a texture map whose resolution is  $L \times W$ , the corresponding pixel index of  $(u, v)$  is

$$x = u \times L, y = (1 - v) \times W. \quad (3)$$

Each spatial face is textured by a 2D texture area consisting of a group of pixels [35], [36]. Using a triangle face as an example, the coordinates of the three vertex pixels are  $(x_1, y_1)$ ,  $(x_2, y_2)$ , and  $(x_3, y_3)$ , circling a triangle on the texture map with a cluster of pixels contained, i.e.,

$$\mathcal{T}_{i, \mathbf{G}_{k, \mathbf{M}}} = \{p_{x, y}\} \subset \text{Tri}[(\mathbf{x}_1, \mathbf{y}_1), (\mathbf{x}_2, \mathbf{y}_2), (\mathbf{x}_3, \mathbf{y}_3)]. \quad (4)$$

The face-wise pixel cluster,  $\mathcal{T}_{i, \mathbf{G}_{k, \mathbf{M}}}$ , circled by a 2D triangle  $\text{Tri}[(\mathbf{x}_1, \mathbf{y}_1), (\mathbf{x}_2, \mathbf{y}_2), (\mathbf{x}_3, \mathbf{y}_3)]$  transformed by the three vertex texture coordinates of the  $i$ th face from the 1-hop geodesic patch  $\mathbf{G}_{k, \mathbf{M}}$ , is formulated in Eq. (4), with  $\{p_{x, y}\}$  representing the pixels used to texture  $i$ th face. For the whole 1-hop geodesic patch, we have a patch pixel cluster

$$\mathcal{T}_{\mathbf{G}_{k, \mathbf{M}}} = \{\mathcal{T}_{i, \mathbf{G}_{k, \mathbf{M}}}\}, i \in |\mathcal{F}_{\mathcal{V}_{(v, k)}}|, \quad (5)$$

$|\mathcal{F}_{\mathcal{V}_{(v, k)}}|$  represents the number of faces in the corresponding 1-hop geodesic patch.

After patch texture mapping, each 1-hop geodesic patch, i.e.,  $\mathbf{G}_{k, \mathbf{M}}$ , has a patch pixel cluster  $\mathcal{T}_{\mathbf{G}_{k, \mathbf{M}}}$ . To distinguish the patch that only has geometry information, we note the 1-hop geodesic patch with patch pixel cluster as the 1-hop textured geodesic patch, i.e.,  $\mathbf{TG}_{k, \mathbf{M}} = \mathbf{G}_{k, \mathbf{M}} \oplus \mathcal{T}_{\mathbf{G}_{k, \mathbf{M}}}$ .

#### F. Feature extraction

Three types of feature are extracted from  $\mathbf{TG}_{k, \mathbf{M}}$  to quantify the influence of distortion on human perception: patch color smoothness, patch discrete mean curvature, and patch pixel color average and variance.

1) *Patch color smoothness*: Patch color smoothness is inspired by the GSP theory [37], which can reflect the signal values differences between neighboring vertices and has been widely used in image and point cloud denoising [38], [39].

Human perception is sensitive to high-frequency distortion, such as edge, contour, and texture gradient [40], motivating the graph representation of the 1-hop mesh geodesic patch to facilitate measurement of high-frequency features. An adjacency matrix,  $\mathcal{W}$ , is first constructed as

$$\mathbf{W}_{v_i, v_j} = \begin{cases} e^{-\frac{\|v_i - v_j\|^2}{2\sigma}} & \text{if } (v_i, v_j) \in \mathcal{F}_{\mathcal{V}_{(v, k)}}, \\ 0 & \text{otherwise.} \end{cases} \quad (6)$$

Two vertices,  $v_i$  and  $v_j$ , have an edge weight  $\mathbf{W}_{v_i, v_j}$  if they were indicated with a definite connection relationship in the face matrix, i.e.,  $(v_i, v_j) \in \mathcal{F}_{\mathcal{V}_{(v, k)}}$ . Then the degree matrix,  $\mathcal{D}$ , used to measure the edge density of each vertex, is a diagonal matrix calculated by  $\mathcal{D} = \text{diag}(d_1, \dots, d_n) \in \mathbb{R}^{n \times n}$ ,  $d_i = \sum_{v_j} \mathbf{W}_{v_i, v_j}$ ,  $n$  is the number of vertex in  $\mathbf{G}_{k, \mathbf{M}}$ .

Both  $\mathcal{W}$  and  $\mathcal{D}$  lead to the graph Laplacian matrix,

$$\mathcal{L} = \mathcal{D} - \mathcal{W}, \quad (7)$$

which is a difference operand on graph. The normalized form of  $\mathcal{L}$  is defined as  $\mathcal{L}' = \mathcal{D}^{-\frac{1}{2}} \mathcal{L} \mathcal{D}^{\frac{1}{2}}$  [37].

For each vertex in  $\mathbf{TG}_{k, \mathbf{M}}$ , the three-channel RGB color information is provided with the pixel cluster. Considering YUV color space is suggested to be much closer related to human perception, a color space conversion is applied to generate graph signals as

$$f = [f_1, f_2, f_3] = [Y, U, V] = \text{rgb2yuv}([R, G, B]), \quad (8)$$

$\text{rgb2yuv}(\cdot)$  realizes the color space conversion from  $[R, G, B]$  to  $[Y, U, V]$ .

The patch color smoothness for signal  $f_i \in \mathbb{R}^{n \times 1}$ ,  $i = 1, 2, 3$ , is formulated as

$$\mathbf{F}_i^{\text{PCS}} = \frac{f_i^T \mathcal{L}' f_i}{|\mathcal{T}_{\mathbf{G}_{k, \mathbf{M}}}|}. \quad (9)$$

$|\mathcal{T}_{\mathbf{G}_{k, \mathbf{M}}}|$  is the number of pixels in  $\mathcal{T}_{\mathbf{G}_{k, \mathbf{M}}}$ , covered by  $\mathbf{G}_{k, \mathbf{M}}$  on the texture map.

$f_i^T \mathcal{L}' f_i$  is the Laplacian quadratic form of the graph in GSP, which is the integral of the gradient of the edge of the graph, appreciated for measuring the global smoothness of the signal [37]. Unlike the general representation of the graph in GSP,  $\mathcal{T}_{\mathbf{G}_{k, \mathbf{M}}}$  is not a hollow graph with only vertices and edges. Regarding the definition of edge gradient in GSP, the number of effective pixels is used to normalize  $f_i^T \mathcal{L}' f_i$  and infer the patch color smoothness.

2) *Patch discrete mean curvature*: Patch discrete mean curvature is inspired by the intuition that the human visual system processes color and form separately [17], which can reflect the geometric mean curvature of the patch center. Patch color smoothness is mainly oriented to color features and only considers the influence of the Euclidean distance of the vertex while the spatial motion / orientation of the vertex is undervalued [15]. To accurately infer the characteristics of the patch geometry, the discrete mean curvature of the patch is consequently calculated.

To measure geometry deformation with respect to 3D space, the Laplace-Beltrami operand (LBO), which is the manifold generalization of the Laplace operand, is proposed [41]. The Cotangent formula of LBO (Cot-LBO) is defined as

$$\mathcal{L}_i^{\text{Cot}} = \frac{1}{2A_i} \sum_{v_j} [\cot(\alpha_{i, j}) + \cot(\beta_{i, j})](f(v_i) - f(v_j)), \quad (10)$$

$\cot(\alpha_{i, j})$  and  $\cot(\beta_{i, j})$  are the cotangent values of two diagonals corresponding to edge  $(v_i, v_j)$ .  $A_i$  is the local averaging area of  $v_i$ , such as the barycentric cell, the Voronoi cell and the mixed Voronoi cell.

The essence of Cot-LBO is a vector in  $v_i$ , sharing the same magnitude with vertex mean curvature when  $f(v) = v$  [42], it then leads to the discrete mean curvature  $F_i^{\text{dmc}}$  of  $v_i$ :

$$|\mathcal{L}_i^{\text{Cot}}| = |-2F_i^{\text{dmc}} \cdot N|, \quad (11)$$

$$\because F_i^{\text{dmc}} \geq 0, \quad (12)$$

$$F_i^{\text{dmc}} = \frac{|\mathcal{L}_i^{\text{Cot}} \cdot N|}{2}. \quad (13)$$



$N$  is the normalized normal vector at  $v_i$ , and we use the discrete mean curvature at the patch center to represent the patch discrete mean curvature, i.e.,  $F^{dmc} = F_k^{dmc}$ .

3) *Patch pixel color average and variance*: Both patch color smoothness and discrete mean curvature are highly dependent on vertices, while texture inside the face is ignored. Therefore, the characteristics of textured faces are thus measured by patch pixel color average and variance, which can reflect the statistical features of face texture, i.e., mean and variance of luminance and chrominance.

Inspired by SSIM [22], the effective pixels of each face are analogized to the pixel window that is widely used in IQA. For the  $i$ th face-wise pixel cluster,  $\mathcal{T}_{i,G_{k,M}}$ , of the patch pixel cluster  $\mathcal{T}_{G_{k,M}}$ ,

$$\mathcal{T}_{i,G_{k,M}} = \{p_{x,y}\} = \{[Y, U, V]_j\}, j = 1, 2, \dots, m. \quad (14)$$

Each pixel provides a color information tuple  $[Y, U, V]_j$  after the same color space conversion as Eq. (8), and  $m$  represents the number of pixels used to render the texture of  $i$ th face. Channel-wise luminance and chrominance average and variance are derived as

$$\bar{C}_i = \frac{1}{M} \sum_j [C]_j, C_i^2 = \frac{1}{M} \sum_j ([C]_j - \bar{C}_i)^2, C \in \{Y, U, V\}. \quad (15)$$

Patch pixel color average and variance are finally calculated via pooling all the face results, i.e.,

$$\begin{aligned} F_1^{pca} &= \frac{\sum_i s_i \bar{Y}_i}{\sum_i s_i}, F_2^{pca} = \frac{\sum_i s_i \bar{U}_i}{\sum_i s_i}, F_3^{pca} = \frac{\sum_i s_i \bar{V}_i}{\sum_i s_i}, \\ F_1^{pcv} &= \frac{\sum_i s_i Y_i^2}{\sum_i s_i}, F_2^{pcv} = \frac{\sum_i s_i U_i^2}{\sum_i s_i}, F_3^{pcv} = \frac{\sum_i s_i V_i^2}{\sum_i s_i}. \end{aligned} \quad (16)$$

(17)

$s_i$  are the weighting factors between the faces, which are set according to the number of effective pixels of the face.

### G. Feature pooling

For each  $\mathcal{T}_{G_{k,M}}$ , we have patch color smoothness  $F^{pcs}$ , patch discrete mean curvature  $F^{dmc}$ , and patch pixel color average and variance  $F^{pca}$  and  $F^{pcv}$ .  $F^{pcs}$ ,  $F^{pca}$  and  $F^{pcv}$  are three triples corresponding to three color channels. Eq. (18) is proposed to measure the similarity of features extracted from patches constructed by keypoint  $k$  from the reference and distorted meshes.

$$\text{SIM}_k^F = \frac{|2F_r \cdot F_d| + T}{(F_r)^2 + (F_d)^2 + T}. \quad (18)$$

$T$  is a small non-zero constant to prevent numerical instability,  $F \in \{F_i^{pcs}, F^{dmc}, F_i^{pca}, F_i^{pcv}\}$ ,  $i \in \{1, 2, 3\}$ .

A simple average pooling is first adopted to fuse feature similarities between multiple texture 1-hop geodesic patches,

$$\text{SIM}^F = \frac{1}{|\mathcal{K}|} \sum_{k \in \mathcal{K}} \text{SIM}_k^F. \quad (19)$$

$\text{SIM}^{F^{dmc}}$  can be calculated directly using Eq. (20), e.g.,

$$\text{SIM}^{F^{dmc}} = \frac{1}{|\mathcal{K}|} \sum_{k \in \mathcal{K}} \text{SIM}_k^{F^{dmc}}. \quad (20)$$

Then weighting factors  $\{\gamma_i\}_{i=1,2,3}$  are used to pooling triple features of  $F^{pcs}$ ,  $F^{pca}$  and  $F^{pcv}$  [43], e.g.,

$$\text{SIM}^F = \frac{1}{\gamma} \sum_i \gamma_i \cdot \text{SIM}^{F_i}, i \in \{1, 2, 3\}, \quad (21)$$

where  $\gamma_i$  is the pooling factor of  $i$ -channel reflecting the importance of individual color channels during visual perception,  $\gamma = \sum_i \gamma_i$ .

In the end, we have the overall mesh quality by averaging feature similarities:

$$Q = \frac{1}{4} [\text{SIM}^{F^{pcs}} + \text{SIM}^{F^{dmc}} + \text{SIM}^{F^{pca}} + \text{SIM}^{F^{pcv}}]. \quad (22)$$

## V. EXPERIMENTAL EVALUATIONS

This section first evaluates GeodesicPSIM and other SOTA metrics in the database introduced in section III, exhibiting the superiority of the proposed GeodesicPSIM. Then, the robustness of GeodesicPSIM is explored with different hyperparameter settings. The ablation study, presented in the last, demonstrates the importance of fusing three types of features and patch cropping.

### A. Metric parameters

GeodesicPSIM has some hyperparameters and adaptive operands that need to be determined before application, leading to the following elaboration:

- $\phi[*]$ ,  $kn$  in *keypoint selection*:  $kn = 500$  and two different sampling methods are used to compare the importance of keypoint selection, i.e., random sampling (RS) and farthest point sampling (FPS).
- $\tau$  in *patch cropping*:  $\tau = 0.5 \times 10e^{-3} \times \text{Bbox}$ ,  $\text{Bbox} = \max(X_s, Y_s, Z_s)$  with  $X_s = X_{\max} - X_{\min}$ ,  $Y_s = Y_{\max} - Y_{\min}$  and  $Z_s = Z_{\max} - Z_{\min}$  as respective bounding box scale of  $x$ -,  $y$ -, and  $z$ -axis of reference mesh.
- $\sigma$  in *patch color smoothness*:  $\sigma$  is determined using the averaged Euclidean distance between vertices that have edges defined in  $\mathcal{F}_{V(v,k)}$ .
- $A_i$  in *patch discrete mean curvature*: Voronoi cell is used as a local averaging area to calculate Cot-LBO.
- $T$ ,  $\gamma_i$  in *feature pooling*:  $T$  is set to  $2.22 \times e^{-16}$ , which is the minimal floating number defined in MATLAB software.  $[\gamma_1, \gamma_2, \gamma_3] = [6, 1, 1]$  to reflect the different importance of various color components as proposed in PSNR<sub>yuv</sub> [43], in which luminance is more sensitive to HVS.

### B. SOTA metric introduction

Three types of SOTA metrics are introduced, which will be used as comparative baselines to highlight the superiority of GeodesicPSIM: image-based, point-based, and video-based metrics.

1) *Image-based metrics*: Image-based metrics, proposed by WG 7 [10], are based on the images projected from 16 viewpoints resulting from the Fibonacci sphere lattice [44]. Three metrics are tested based on the 16 images obtained:  $\text{geo}_{\text{psnr}}$ ,  $\text{rgb}_{\text{psnr}}$ , and  $\text{yuv}_{\text{psnr}}$ .  $\text{geo}_{\text{psnr}}$  calculates the depth information differences between the reference and distorted meshes. The depth information is captured as an image, which pixel values are normalized to 255, to get PSNR values comparable to the ones obtained using the next two metrics.  $\text{rgb}_{\text{psnr}}$  and  $\text{yuv}_{\text{psnr}}$  calculate the differences of (R, G, B) and (Y, U, V) color channels between reference and distorted images. Color information is captured as an image. In this paper, the resolution of projected images is set as  $1920 \times 1920$ . A more detailed description of the metrics can be found in [10].

2) *Point-based metrics*: The point-based metrics are based on sampled point clouds from meshes. Seven point cloud quality metrics are evaluated: D1 [18], D2 [19],  $\text{PSNR}_{\text{yuv}}$  [43], PointSSIM [45], MPED [29],  $\text{PCQM}_{\text{psnr}}$  [20] [10], and GraphSIM [15]. As [10] reported that grid sampling has a stable behavior, it is used in this section with a grid resolution of 1024 to generate the colored point clouds.

3) *Video-based metric*: The video-based metrics are based on PVSs displayed during the subjective experiment [46]. The MSU Video Quality Measurement Tool [47] is used to compute the following IQA/VQA metrics: PSNR, SSIM [22], MSSIM [12], 3SSIM [48], VQM [49], and VMAF [23]. PVSs have  $1920 \times 1080$  resolution and a duration of 18 seconds.

### C. Performance of objective metrics

To ensure the consistency between subjective scores (e.g., MOS) and objective predictions from various metrics, the objective predictions of different metrics are mapped to the same dynamic range following the recommendations suggested by the video quality experts group [50]. Three performance correlation indicators are employed to quantify the efficiency of the objective metrics: PLCC, SRCC, and RMSE. PLCC can demonstrate prediction accuracy, SRCC can reflect prediction monotonicity, and RMSE can show prediction consistency. More details can be found in [50].

1) *Correlation of objective metric*: We report the results of PLCC, SRCC, and RMSE on the whole database in columns "All" of Table III. GeodesicPSIM (FPS) reports the best performance, which is the one and only metric that PLCC and SRCC are higher than 0.8, followed by GeodesicPSIM (RS), GraphSIM,  $\text{PCQM}_{\text{psnr}}$ , and  $\text{geo}_{\text{psnr}}$ .

Fig. 8 shows the scatter plots of  $\text{rgb}_{\text{psnr}}$ , D1,  $\text{PCQM}_{\text{psnr}}$ , VMAF, GeodesicPSIM (RS) and GeodesicPSIM (FPS). Points away from the best-fit logistic regression curve, colored in yellow, illustrating the bad prediction cases for each metric: GeodesicPSIM has the best scatter plot, with the yellow curve close to the perfect case " $y = x$ ". D1 reports several failed predictions with extreme value differences with MOSs, such as  $D1 = 3.5$  vs.  $\text{MOS} = 1.0$ ,  $D1 = 1.5$  vs.  $\text{MOS} = 4.5$ , etc. VMAF tend to score lower for high-quality meshes.  $\text{rgb}_{\text{psnr}}$  has less outliers than  $\text{PCQM}_{\text{psnr}}$  but reports poorer

TABLE III: Metric performance on TSMD.

Type	Metric	All			AOMedia Classes							Creation	
		PLCC	SRCC	RMSE	A2	B	D-1	D-2	E	F	DCC	3DS	
A	$\text{geo}_{\text{psnr}}$	0.73	0.73	0.80	0.92	0.90	0.72	0.71	0.87	0.74	<b>0.93</b>	0.73	
	$\text{rgb}_{\text{psnr}}$	0.69	0.67	0.84	0.86	0.84	0.77	0.89	0.74	0.80	0.87	0.72	
	$\text{yuv}_{\text{psnr}}$	0.68	0.68	0.85	0.85	0.83	0.76	0.88	0.76	0.80	0.86	0.72	
B	D1	0.72	0.65	0.80	0.93	<b>0.95</b>	0.73	0.68	0.65	0.77	0.92	0.71	
	D2	0.54	0.47	0.98	0.84	0.93	0.69	0.52	0.48	0.44	0.85	0.54	
	$\text{PSNR}_{\text{yuv}}$	0.60	0.60	0.93	0.69	0.79	0.66	0.85	0.63	0.79	0.69	0.64	
	MPED	0.48	0.50	1.01	0.56	0.39	0.44	0.50	0.66	0.75	0.52	0.48	
	PointSSIM	0.48	0.41	1.02	0.85	0.52	0.56	0.72	0.59	0.43	0.75	0.46	
	$\text{PCQM}_{\text{psnr}}$	0.76	0.75	0.76	0.85	0.85	0.81	<b>0.91</b>	0.76	0.89	0.82	0.78	
	GraphSIM	0.79	0.79	0.70	0.90	0.85	0.86	0.77	0.77	0.96	0.91	0.78	
C	PSNR	0.53	0.54	0.99	<b>0.95</b>	0.55	0.66	0.65	0.80	0.44	0.86	0.55	
	SSIM	0.51	0.67	0.85	0.78	0.53	0.64	0.63	0.74	0.52	0.74	0.48	
	MSSIM	0.66	0.65	0.87	0.92	0.51	0.77	0.74	0.89	0.54	0.86	0.64	
	3SSIM	0.68	0.67	0.85	0.94	0.52	0.83	0.73	0.93	0.52	0.91	0.69	
	VQM	0.67	0.67	0.86	0.89	0.66	0.74	0.74	0.89	0.51	0.87	0.69	
	VMAF	0.70	0.51	1.00	0.94	0.63	0.79	0.76	<b>0.91</b>	0.61	0.87	0.69	
	GeodesicPSIM (RS)	0.80	0.80	0.69	0.81	0.86	<b>0.83</b>	0.80	0.86	0.88	0.82	0.81	
	GeodesicPSIM (FPS)	<b>0.82</b>	<b>0.82</b>	<b>0.66</b>	0.82	0.87	0.79	0.81	0.88	<b>0.95</b>	0.82	<b>0.82</b>	

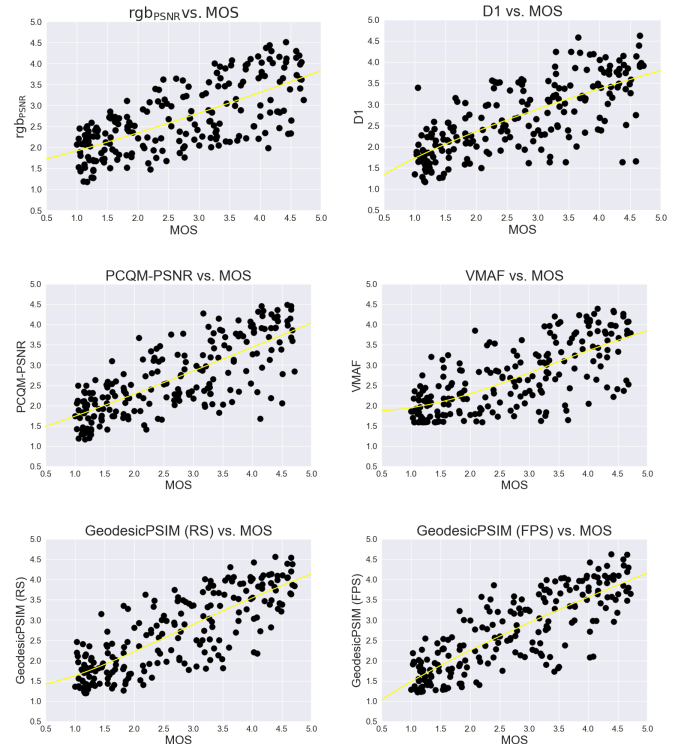


Fig. 8: Scatter plots of metrics.

quantified correlations, which seems contradictory, resulting in the analysis by content category exhibited in the next section.

2) *Analysis by category of content*: For a more in-depth analysis of the metric performance, the whole database is split into subclasses, sharing close characteristics or creation processes for each, with PLCC reported in columns "AOMedia Classess" and "Creation". Six different subclasses are defined

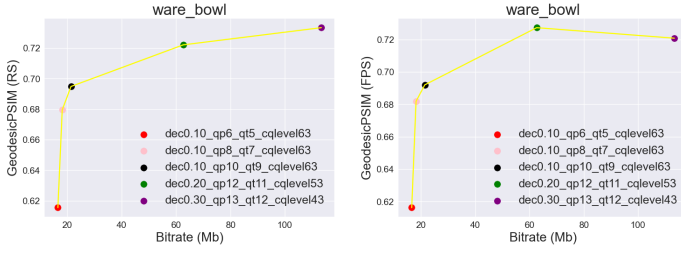


Fig. 9: GeodesicPSIM scores vs bitrate curves.

in AOMedia VVM CfP [1]. A2 collects game characters obtained by digital content creation (DCC), B is a collection of avatars captured as 3D scans (3DS) of humans, D consists of professional 3DS (D-1 with only triangular faces and D-2 with any polygonal faces), E contains non-professional 3DS of objects, and F professional 3DS from outdoor and indoor scenes. DCC and 3DS, which indicate the creation process of the meshes, also used as index to split database, the results are consequently reported in columns "Creation".

It is observed that the metrics that have the best "All" performance tend to present close results among different classes. Almost all the correlations of GeodesicPSIM are higher than 0.80 and it demonstrates the best results on classes D-1, F, and 3DS.  $rgb_{psnr}$  shows close performance with  $yuv_{psnr}$  regardless of subclasses, indicating that the influence of color space is limited on pixel-wise metrics. D1 and D2 report the highest correlation on class B, revealing that they may be better suited for evaluating human figure meshes.  $PCQM_{psnr}$  reports better correlation than  $rgb_{psnr}$  in classes F and 3DS ( $\Delta PLCC > 0.05$ ), giving the reason that  $PCQM_{psnr}$  has a higher "All". Some video-based metrics show impressive results in classes A2 and E, with correlations above 0.90, but fail utterly in classes B and F. The score magnitude of video-based metrics is easily influenced by the proportion of background content in each video frame, which is not robust among different types of meshes, consequently resulting in performance gap for different classes. For instance, scores for indoor meshes are generally lower than scores for other meshes. The proportion of background content, static and artifact-free, contained in the frame significantly affects the range of quality scores. The frame for indoor meshes has no such background because the inside of the building covers the full frame. It consequently has more distorted information counted by the metrics, leading to a lower quality score.

3) *Extended analysis of GeodesicPSIM*: GeodesicPSIM (FPS) reports superior or close performance than GeodesicPSIM (RS), demonstrating that FPS is a better sampling method than RS for GeodesicPSIM, while an exception is class D-1. After examining the correlation between objective scores and bitrate, the reason is illustrated in Fig. 9. GeodesicPSIM (RS) curve shows perfect monotony, appreciating the intuition that a higher bitrate is supposed to indicate a more detailed visual feature, resulting in a higher objective score, but GeodesicPSIM (FPS) gives non-monotonic results for the meshes labeled by the green and purple points.

Snapshots of the mesh and keypoint sampling results, cor-

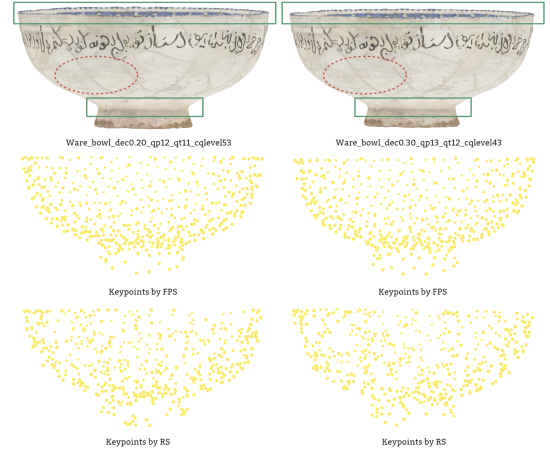


Fig. 10: Keypoints sampling of "Ware\_bowl".

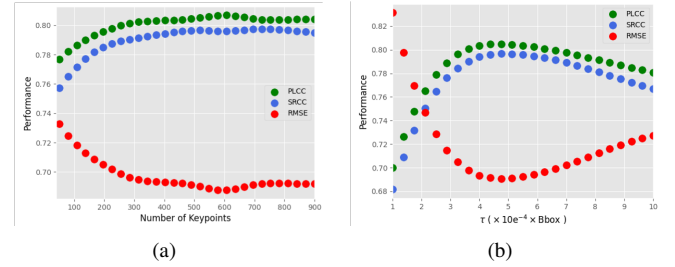


Fig. 11: (a): Metric performance with different number of keypoints; (b): Metric performance with different cropping thresholds.

responding to the green and purple points, are illustrated in Fig. 10. Attractive visual distortion is primarily concentrated in smooth regions, such as the area located in the red circle, but the FPS selects more keypoints distributed in the contour regions indicated by the green rectangles. It consequently has inconsistent attention between FPS keypoints selection and human perception, leading to non-monotonic results.

#### D. Robustness of GeodesicPSIM

The robustness of GeodesicPSIM is evaluated in terms of the number of keypoint, the source of the keypoint, and the size of the 1-hop geodesic patch.

1) *The number of keypoint*: Keypoints play a vital role in GeodesicPSIM, maintaining the subsequent 1-hop geodesic patch construction and feature extraction. The performance of using a different number of keypoints to calculate GeodesicPSIM (RS) is reported in Fig. 11 (a). The correlations gradually increase up to around 0.80 for PLCC and SRCC, 0.65 for RMSE, as the number of keypoints reaches 500, and subsequently remain relatively stable, which demonstrates the model generalization with enough keypoints collected.

2) *The source of keypoint*: The keypoints are derived from distorted meshes initially, assuming that the vertices belonging to distorted meshes are more appropriate to find a closer neighbor in the reference meshes, to facilitate building a local area correspondence. To verify whether the above hypothesis leads

to a significant improvement in the performance of the metric, the results of using FPS and RS to sample 500 keypoints from different sources are reported in Table IV. For a larger 1-hop geodesic patch,  $\tau = 0.5 \times 10e^{-2}$ , FPS shows better performance than RS regardless of the source of keypoints. For a smaller 1-hop geodesic patch,  $\tau = 0.5 \times 10e^{-3}$ , FPS demonstrates slightly better results than RS when keypoints derived from distorted meshes, while close results using keypoints from reference meshes. The source of keypoints have limited influence on the metric performance regardless of sampling methods, different from the hypothesis established, which indicates that GeodesicPSIM does not require a strict local area matching, and consequently prove the robustness of the metric.

TABLE IV: Metric performance with different keypoint sources.

Source	Method	$\tau = 0.5 \times 10e^{-2}$			$\tau = 0.5 \times 10e^{-3}$		
		PLCC	SRCC	RMSE	PLCC	SRCC	RMSE
Reference	RS	0.76	0.75	0.76	0.82	0.81	0.67
	FPS	0.80	0.79	0.69	0.82	0.82	0.66
Distortion	RS	0.75	0.74	0.77	0.80	0.80	0.69
	FPS	0.80	0.79	0.70	0.82	0.82	0.66

3) *The size of 1-hop geodesic patch*: 1-hop geodesic patch is the basic unit for quality prediction, which is sliced from the mesh surface. Given  $\tau$  to control patch size, GeodesicPSIM fuses feature similarities on certain scales to infer quality scores. The performance of GeodesicPSIM (RS) with respect to different  $\tau$  is illustrated in Fig. 11 (b). It reveals that the performance of the metric can be quickly improved by enlarging the patch size, reaching the highest correlation with PLCC and SRCC = 0.80 when  $\tau$  around  $4.5 \times 10e^{-4} \times \text{Bbox}$ , and then slowly decrease. The curve implies that a proper patch size is extremely important for effective feature extraction.

#### E. Ablation study

This section examines GeodesicPSIM by reassembling its modules to report its efficiency.

1) *Feature extraction*: GeodesicPSIM pools three types of features, that is, patch color smoothness  $F^{pcs}$ , patch discrete mean curvature  $F^{dmc}$ , and patch pixel color average and variance  $F^{pca}$  and  $F^{pcv}$ , to infer mesh quality. To validate feature effectiveness, the performance of the individual features and the pair is reported in Table V.  $F^{dmc}$  exhibits the best results, followed by  $F^{pcs}$ , and  $F^{pca}$  and  $F^{pcv}$ . Each feature contributes to the overall performance of GeodesicPSIM, regarding the results of pairwise feature combinations that are poorer than GeodesicPSIM (RS).

2) *Patch cropping*: The importance of patch size has been validated in Section V-D3, for which patch cropping is the assurance. The effectiveness of two patch cropping steps: the first step for ensuring a close patch size between reference and distorted meshes; and the second step for a proper patch size, is shown in Table VI. Both two cropping steps improve the overall performance of the metric, again confirming the importance of proper patch size.

TABLE V: Feature effectiveness of GeodesicPSIM.

Features Combination	PLCC	SRCC	RMSE
$F^{pcs}$	0.52	0.47	0.99
$F^{dmc}$	0.68	0.66	0.85
$F^{pca}$ and $F^{pcv}$	0.36	0.35	1.08
$F^{pcs} + F^{dmc}$	0.72	0.72	0.80
$F^{dmc} + F^{pca}$ and $F^{pcv}$	0.65	0.64	0.88
$F^{pcs} + F^{pca}$ and $F^{pcv}$	0.72	0.70	0.81
GeodesicPSIM (RS)	0.80	0.80	0.69

TABLE VI: Metric performance without patch cropping.

	PLCC	SRCC	RMSE
No Cropping Step 1 and No Cropping Step 2	0.71	0.69	0.82
Cropping Step 1 and No Cropping Step 2	0.73	0.72	0.79
Cropping Step 1 and Cropping Step 2	0.80	0.80	0.69

## VI. CONCLUSIONS

In this paper, we propose a new model-based static mesh objective quality metric, called GeodesicPSIM. GeodesicPSIM consists of seven steps: mesh cleaning, keypoint selection, 1-hop geodesic patch construction, patch cropping, patch texture mapping, feature extraction, and feature pooling. We have used a newly created and challenging database, TSMD, to validate the superiority of GeodesicPSIM, on which GeodesicPSIM reports PLCC, SRCC, and RMSE at 0.82, 0.82, and 0.66, ranking first among all metrics tested. The robustness of GeodesicPSIM is examined by checking the performance variation in terms of different high-parameter settings, and ablation studies have shown the effectiveness of the three types of feature proposed and the novel patch cropping module.

There are many expected tracks for future study. First, quality metrics for image, video, and point clouds have reported PLCC and SRCC above 0.90 on some databases, inspiring us to continue to improve the performance of GeodesicPSIM. Second, considering GeodesicPSIM is a full-reference metric that requires the injection of reference meshes, an effective no-reference metric needs to be designed to deal with the cases where the reference meshes are not available.

## REFERENCES

- [1] VVM, "Call for proposals on static polygonal mesh coding," *Alliance for Open Media, document: VVM-2023-0040-v2*, 2023.
- [2] I. Kompatsiaris, D. Tzovaras, and M. Strintzis, "Hierarchical representation and coding of surfaces using 3-d polygon meshes," *IEEE Trans. Image Processing*, vol. 10, no. 8, pp. 1133–1151, 2001.
- [3] J.-H. Yang, C.-S. Kim, and S.-U. Lee, "Semi-regular representation and progressive compression of 3-d dynamic mesh sequences," *IEEE Trans. Image Processing*, vol. 15, no. 9, pp. 2531–2544, 2006.
- [4] J. Peng, C.-S. Kim, and C.-C. J. Kuo, "Technologies for 3d mesh compression: A survey," *Journal of visual communication and image representation*, vol. 16, no. 6, pp. 688–733, 2005.
- [5] G. Lavoué, E. D. Gelasca, F. Dupont, A. Baskurt, and T. Ebrahimi, "Perceptually driven 3d distance metrics with application to watermarking," *Applications of Digital Image Processing XXIX*, vol. 6312, pp. 150–161, 2006.
- [6] M. Corsini, E. D. Gelasca, T. Ebrahimi, and M. Barni, "Watermarked 3-d mesh quality assessment," *IEEE Trans. Multimedia*, vol. 9, no. 2, pp. 247–256, 2007.
- [7] Z. Karni and C. Gotsman, "Spectral compression of mesh geometry," *Proc. conf. Computer Graphics and Interactive Techniques*, pp. 279–286, 2000.



- [8] L. Váša and J. Rus, "Dihedral angle mesh error: a fast perception correlated distortion measure for fixed connectivity triangle meshes," *Computer Graphics Forum*, vol. 31, no. 5, pp. 1715–1724, 2012.
- [9] P. Cignoni, C. Rocchini, and R. Scopigno, "Metro: measuring error on simplified surfaces," *Computer Graphics Forum*, vol. 17, no. 2, pp. 167–174, 1998.
- [10] WG7, "Metrics for dynamic mesh coding," *ISO/IEC JTC 1/SC 29/WG 7, MPEG 3D Graphics Coding, WG7 N0225*, 2021.
- [11] Y. Nehmé, F. Dupont, J.-P. Farrugia, P. Le Callet, and G. Lavoué, "Visual quality of 3d meshes with diffuse colors in virtual reality: Subjective and objective evaluation," *IEEE Trans. Visualization and Computer Graphics*, vol. 27, no. 3, pp. 2202–2219, 2020.
- [12] Z. Wang, E. P. Simoncelli, and A. C. Bovik, "Multiscale structural similarity for image quality assessment," in *IEEE Asilomar Conf. Signals, Systems & Computers*, vol. 2, 2003, pp. 1398–1402.
- [13] Q. Yang, Y. Liu, S. Chen, Y. Xu, and J. Sun, "No-reference point cloud quality assessment via domain adaptation," in *Proc. IEEE/CVF Conf. Computer Vision and Pattern Recognition*, 2022, pp. 21 179–21 188.
- [14] Y. Liu, Q. Yang, Y. Xu, and L. Yang, "Point cloud quality assessment: Dataset construction and learning-based no-reference metric," *ACM Trans. Multimedia Computing, Communications and Applications*, vol. 19, no. 2s, pp. 1–26, 2023.
- [15] Q. Yang, Z. Ma, Y. Xu, Z. Li, and J. Sun, "Inferring point cloud quality via graph similarity," *IEEE Trans. Pattern Analysis and Machine Intelligence*, pp. 1–1, 2020.
- [16] L. Itti, C. Koch, and E. Niebur, "A model of saliency-based visual attention for rapid scene analysis," *IEEE Trans. Pattern Analysis and Machine Intelligence*, vol. 20, no. 11, pp. 1254–1259, 1998.
- [17] I. Rentzperis, A. R. Nikolaev, D. C. Kiper, and C. van Leeuwen, "Distributed processing of color and form in the visual cortex," *Frontiers in psychology*, vol. 5, p. 932, 2014.
- [18] R. Mekuria, Z. Li, C. Tulvan, and P. Chou, "Evaluation criteria for point cloud compression," *ISO/IEC MPEG n16332, Geneva, Switzerland*, Feb, 2016.
- [19] D. Tian, H. Ochimizu, C. Feng, R. Cohen, and A. Vetro, "Geometric distortion metrics for point cloud compression," in *2017 IEEE Int. Conf. Image Processing*, 2017, pp. 3460–3464.
- [20] G. Meynet, Y. Nehmé, J. Digne, and G. Lavoué, "PCQM: A full-reference quality metric for colored 3D point clouds," in *Int. Conf. Quality of Multimedia Experience*, 2020.
- [21] Y. Zhang, Q. Yang, and Y. Xu, "Ms-graphsim: Inferring point cloud quality via multiscale graph similarity," in *Pro. the 29th ACM Int. Conf. Multimedia*, 2021, pp. 1230–1238.
- [22] Z. Wang, A. C. Bovik, H. R. Sheikh, and E. P. Simoncelli, "Image quality assessment: from error visibility to structural similarity," *IEEE Trans. Image Processing*, vol. 13, no. 4, pp. 600–612, 2004.
- [23] Z. Li, A. Aaron, I. Katsavounidis, A. Moorthy, and M. Manohara, "Toward a practical perceptual video quality metric," *The Netflix Tech Blog*, vol. 6, no. 2, p. 2, 2016.
- [24] A. Javaheri, C. Brites, F. Pereira, and J. Ascenso, "Point cloud rendering after coding: Impacts on subjective and objective quality," *IEEE Trans. Multimedia*, vol. 23, pp. 4049–4064, 2021.
- [25] Q. Yang, H. Chen, Z. Ma, Y. Xu, R. Tang, and J. Sun, "Predicting the perceptual quality of point cloud: A 3d-to-2d projection-based exploration," *IEEE Trans. Multimedia*, vol. 23, pp. 3877–3891, 2021.
- [26] Q. Yang, J. Jung, H. Wang, X. Xu, and S. Liu, "Tsmc: A database for static color mesh quality assessment study," *arXiv preprint arXiv:2308.01940*, 2023.
- [27] J. Jung, M. Wien, and V. Baronini, "Draft guidelines for remote experts viewing sessions (v2)," *ISO/IEC JTC 1/SC 29/AG 5 M57896*, 2021.
- [28] P. ITU-T RECOMMENDATION, "Subjective video quality assessment methods for multimedia applications," *International Telecommunication Union*, 1999.
- [29] Q. Yang, Y. Zhang, S. Chen, Y. Xu, J. Sun, and Z. Ma, "Mped: Quantifying point cloud distortion based on multiscale potential energy discrepancy," *IEEE Trans. Pattern Analysis and Machine Intelligence*, vol. 45, no. 5, pp. 6037–6054, 2023.
- [30] WG7, "Anchors for dynamic mesh coding evaluation," *ISO/IEC JTC 1/SC 29/WG 7, MPEG 3D Graphics Coding, WG7 N0278*, 2022.
- [31] W. Hu, J. Pang, X. Liu, D. Tian, C.-W. Lin, and A. Vetro, "Graph signal processing for geometric data and beyond: Theory and applications," *IEEE Trans. Multimedia*, vol. 24, pp. 3961–3977, 2021.
- [32] E. P. Simoncelli and B. A. Olshausen, "Natural image statistics and neural representation," *Annual Review of Neuroscience*, vol. 24, no. 1, pp. 1193–1216, 2001.
- [33] D. L. Yamins and J. J. DiCarlo, "Using goal-driven deep learning models to understand sensory cortex," *Nature Neuroscience*, vol. 19, no. 3, p. 356, 2016.
- [34] L. N. Thibos, "Image processing by the human eye," in *Visual Communications and Image Processing IV*, vol. 1199. International Society for Optics and Photonics, 1989, pp. 1148–1153.
- [35] M. Sarkis and K. Diepold, "Content adaptive mesh representation of images using binary space partitions," *IEEE Trans. Image Processing*, vol. 18, no. 5, pp. 1069–1079, 2009.
- [36] X. Yang, G. Lin, and L. Zhou, "Single-view 3d mesh reconstruction for seen and unseen categories," *IEEE Trans. Image Processing*, vol. 32, pp. 3746–3758, 2023.
- [37] D. I. Shuman, S. K. Narang, P. Frossard, A. Ortega, and P. Vandergheynst, "The emerging field of signal processing on graphs: Extending high-dimensional data analysis to networks and other irregular domains," *IEEE Signal Processing Magazine*, vol. 30, no. 3, pp. 83–98, 2013.
- [38] J. Zeng, G. Cheung, M. Ng, J. Pang, and C. Yang, "3D point cloud denoising using graph laplacian regularization of a low dimensional manifold model," *IEEE Trans. Image Processing*, 2019.
- [39] Y. Bai, G. Cheung, X. Liu, and W. Gao, "Graph-based blind image deblurring from a single photograph," *IEEE Trans. Image Processing*, vol. 28, no. 3, pp. 1404–1418, 2018.
- [40] Q. Yang, Z. Ma, Y. Xu, L. Yang, W. Zhang, and J. Sun, "Modeling the screen content image quality via multiscale edge attention similarity," *IEEE Trans. Broadcasting*, vol. 66, no. 2, pp. 310–321, 2019.
- [41] M. P. Do Carmo, *Differential geometry of curves and surfaces: revised and updated second edition*. Courier Dover Publications, 2016.
- [42] M. Meyer, M. Desbrun, P. Schröder, and A. H. Barr, "Discrete differential-geometry operators for triangulated 2-manifolds," in *Visualization and mathematics III*. Springer, 2003, pp. 35–57.
- [43] E. M. Torlig, E. Alexiou, T. A. Fonseca, R. L. de Queiroz, and T. Ebrahimi, "A novel methodology for quality assessment of voxelized point clouds," in *Applications of Digital Image Processing XLI*, vol. 10752. International Society for Optics and Photonics, 2018, p. 107520I.
- [44] M. Roberts, "How to evenly distribute points on a sphere more effectively than the canonical fibonacci lattice," <http://extremelearning.com.au/evenly-distributing-points-on-a-sphere/>.
- [45] E. Alexiou and T. Ebrahimi, "Towards a point cloud structural similarity metric," in *2020 IEEE Int. Conf. Multimedia & Expo Workshops*, 2020, pp. 1–6.
- [46] Q. Yang, J. Jung, T. Deschamps, X. Xu, and S. Liu, "Tdm: A database for dynamic color mesh subjective and objective quality explorations," *arXiv preprint arXiv:2308.01499*, 2023.
- [47] A. Antsiferova, S. Lavrushkin, M. Smirnov, A. Gushchin, D. S. Votolin, and D. Kulikov, "Video compression dataset and benchmark of learning-based video-quality metrics," *Conf. Neural Information Processing Systems Datasets and Benchmarks Track*, 2022.
- [48] C. Li and A. C. Bovik, "Three-component weighted structural similarity index," *Image quality and system performance VI*, vol. 7242, pp. 252–260, 2009.
- [49] M. Pinson and S. Wolf, "A new standardized method for objectively measuring video quality," *IEEE Trans. Broadcasting*, vol. 50, no. 3, pp. 312–322, 2004.
- [50] VQEG, "Final report from the video quality experts group on the validation of objective models of video quality assessment," [online]. <http://www.its.bldrdoc.gov/vqeg/vqeg-home.aspx>.